12-2020

Toward Understanding Underlying Mechanisms of Drag Reduction in Turbulent Flow Control

Alex Rogge
University of Nebraska-Lincoln, alexander.rogge@huskers.unl.edu

TOWARD UNDERSTANDING UNDERLYING MECHANISMS OF DRAG REDUCTION IN TURBULENT FLOW CONTROL

by

Alexander J. Rogge

A THESIS

Presented to the Faculty of

The Graduate College at the University of Nebraska

In Partial Fulfillment of Requirements

For the Degree of Master of Science

Major: Mechanical Engineering and Applied Mechanics

Under the Supervision of Professor Jae Sung Park

Lincoln, Nebraska

December 2020

TOWARD UNDERSTANDING UNDERLYING MECHANISMS OF DRAG REDUCTION IN TURBULENT FLOW CONTROL

Alexander John Rogge, M.S.

University of Nebraska, 2020

Advisor: Jae Sung Park

The underlying mechanisms of three different flow-control strategies on drag reduction in a turbulent channel flow are investigated by direct numerical simulations. These strategies include the addition of a small concentration of long-chain polymers into a fluid, the incorporation of slip surfaces, and the application of an external body force. While it has been believed that such methods lead to a skin-friction reduction by controlling near-wall flow structures, the underlying mechanisms at play are still not as clear. In this study, a temporal analysis is employed to elucidate underlying drag-reduction mechanisms among these methods. The analysis is based on the lifetime of turbulent phases represented by the active and hibernating phases of a minimal turbulent channel flow. At a similar amount of drag reduction, the polymer and slip methods show a similar mechanism, while the body force method is different. The polymers and slip surfaces cause hibernating phases to happen more frequently, while the duration of active phases is decreased. However, the body forces cause hibernating phases to happen less frequently but prolong its duration to achieve a comparable amount of drag reduction. A possible mechanism behind the body force method is associated with its unique roller-like vortical structures formed near the wall. These structures appear to prevent interactions between inner and outer regions by which individual hibernating

phases are prolonged. It should motivate adaptive flow-control strategies to fully exploit the distinct underlying mechanisms for optimal and robust control of turbulent drag.

Acknowledgements

My colleagues Ethan Davis and Siamak Mirfendereski have been a great help for their assistance and discussions about my research. I would like to thank my advisor Dr. Jae Sung Park for his guidance and insight for my research during my graduate school career. My experience as a graduate student has been invaluable and will continue to utilize the knowledge I have gained from my colleagues and advisor. I would also like to thank Dr. Sangjin Ryu and Dr. George Gogos for being on my thesis committee.

Table of Contents

Table of Figures

CHAPTER 1: INTRODUCTION

1.1 Introduction

The ability to reduce the amount of drag for industries that rely on turbulent flow such as cargo ships, commercial airliners, and oil pipelines is very beneficial in order to reduce cost and save energy. Turbulent flow is fluid that has irregular or chaotic fluctuations in direction and velocity. This flow is commonly found throughout nature, such as wind blowing through the trees or the water flowing in streams and rivers. Turbulent flow is produced by streamwise vortices within the fluid and these vortices are the leading cause of drag within the fluid. Turbulence is caused by a variety of factors such as changes in the boundary's surface, an increase in volumetric flow rate, and external disturbances such as an object obstructing the flow's path.

Coherent structures play an important role in turbulent dynamics when present in wall-bounded turbulent flows [1]. The near-wall coherent structures are closely related to the self-sustaining process of turbulence, which are similar to the staggered, counter-rotating quasi-streamwise vortices that form low- and high-speed streaks [2]. These near-wall structures are responsible for the production of turbulent kinetic energy as they are observed to burst intermittently [3]. The bursting process accounts for over 80% of the total energy in turbulent fluctuations, these near-wall coherent structures are believed to be the dominant structures associated with turbulence production, leading to skin-friction drag [4]. As a result, multiple control strategies have been developed to manipulate the near-wall coherent structures in order to achieve a significant drag reduction [5].

1.2 Literature Review on Flow-Control Strategies

1.2.1 Polymer Additives

The Finitely Extensible Nonlinear Elastic model (FENE-P) was founded by Anton Peterlin and created from the polymer kinetic theory and models the polymer as a finitely extensible nonlinear elastic dumbbell. The dumbbell shape is formed by two beads connected by a spring as in Figure 1, the dumbbell is constantly stretching and contracting as it travels through the fluid and is able to affect the amount of drag present. The Weissenberg number (Wi) is important when discussing polymers, as it is defined by the multiplication of the maximum extensibility and the relaxation time of the polymer [6]. It is believed that polymers are stretched outside of the near-wall turbulence in the viscous sublayer. This stretching creates an effective viscosity and as it moves closer to the viscous sublayer, the turbulent fluctuations increase the thickness of the buffer layer and evidently reduce the amount of friction on the channel walls [7]. Polymer chains unravel at low Wi and expand at high Wi due to the strong biaxial flows that are related to the quasi-streamwise vortices. As the rotational component of the shear flow rotates the polymers, the kinetic energy is transferred to the molecules, and the polymers begin to stretch. As this happens, the quasi-streamwise vortices assist with bringing faster moving fluid toward the wall and the slower moving fluid away [8]. The primary characteristic of solutions with lower Weissenberg numbers is the lifting of the mean velocity profile into the buffer layers and during higher Weissenberg numbers this lift up reaches into the log-law layer [9]. According to Min et al., the polymers store elastic energy and releases it back into the flow as it travels to the buffer and log-law layers [10].

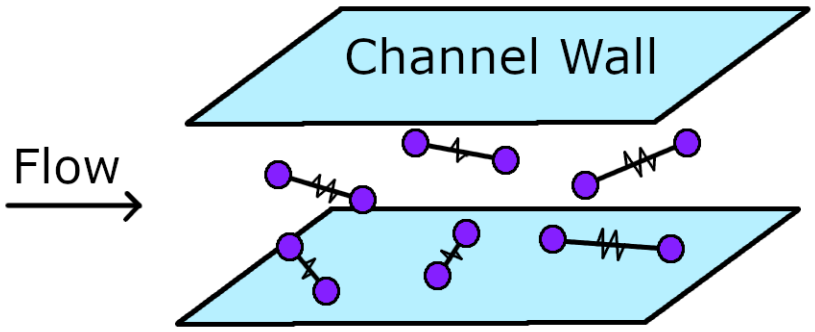

Figure 1: Diagram of polymers within channel flow.

This viscoelasticity weakens the streamwise vortices and can completely suppress coherent structures for larger Weissenberg values. The length of streamwise vortices and the distance between pairs of vortices increases as the drag reduction is increased. These larger coherent structures are much weaker and less numerous in the flow. With the use of polymers, it is possible to achieve approximately 65% drag reduction [6].

For high drag reduction regimes, the vortex structure regeneration becomes suppressed and the vortices tend to remain closer to the wall but become elongated in the direction of the flow. During low drag reduction states, the streak instabilities assist with the regeneration and sustain weak vortices in the flow. As the vortices are lifted, they break apart and cause turbulent fluctuations to appear leading to more instabilities in the fluid. The lift up of vortices is important for transferring the turbulent momentum between the viscous sublayer and log-law layers [9].

1.2.2 Slip Surfaces

Superhydrophobic surfaces are a combination of surface roughness and surface chemistry at the micro and nano scales, recently they have been utilized to produce an

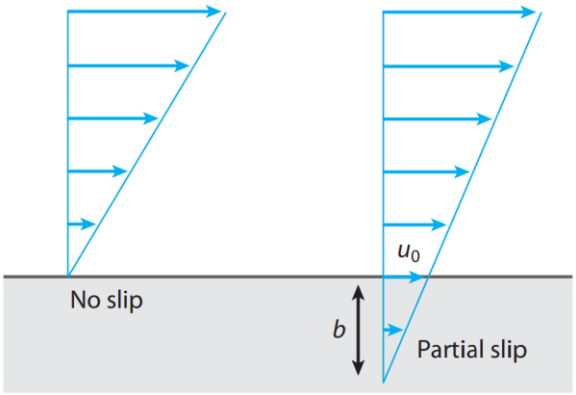

Figure 2: Slip method diagram at solid-fluid interface where *b* corresponds to the slip length [11].

effective slip length on the wall [12]. When water is placed on superhydrophobic surfaces, the water droplet has a contact angle greater than 150 degrees, in return this reduces the amount of free energy at the air-water interface. The superhydrophobic surface can be created by increasing the surface roughness in the micro and nano scales through various processes. On a rough surface, air can be trapped within the valleys to create air pockets that can produce an effective slip length when the surface is completely immersed in water [13]. For direct numerical simulations, instead of simulating the microtextured surface the effective slip length can be predetermined as a system parameter. The diagram in Figure 2 reveals graphically what the induced slip flow is through velocity profiles.

Superhydrophobic surfaces can be implemented experimentally in various ways through equally spaced ridges, posts, microgrates, and also through randomized surface textures [14]. Superhydrophobic surfaces can be used in a variety of different applications such as reducing skin-friction drag, ability to self-clean and reduce the

amount of residue accumulated on a surface, microfluidic devices, and much more. The application we will focus on is the skin-friction drag reduction, which has the potential to increase the amount of energy savings and reduction of greenhouse gas emissions [13].

Drag reduction is achieved differently between laminar and turbulent flows utilizing superhydrophobic surfaces. For laminar flow, drag reduction is a direct result from the effective slip on the surface and its geometry and does not depend on the Reynolds number and other flow conditions. For turbulent flows, the amount of drag reduction was considerably larger than laminar flow when analyzed during experiments. It is viewed that the effective slip length must be on the same order as the viscous sublayer where it is able to alter the streamwise velocity and the wall shear stress fluctuations that occur [13].

When using micrograte as the superhydrophobic surface, the maximum drag reduction was found to be approximately 50% depending on the parameters used. The amount of skin-friction drag also depends on the orientation of the microgrates. In the streamwise direction there is drag reduction, however the spanwise direction led to strong vortices which increased the skin-friction drag [13]. According to Min and Kim from DNS studies, a spanwise slip triggers the transition from laminar to turbulent flow faster and incorporating a streamwise slip delays this transition point [15].

A streamwise slip reduces the shear of the base flow at the wall and causes the velocity profile to flatten, unlike spanwise slip. A reduction in shear stress results in the streamwise vortices and streaks to become weaker. This weakening of vortical structures subdues the streamwise momentum to move them away from the wall, this is known as the lift-up mechanism. If the slip is equal in both the streamwise and spanwise direction,

this is defined as isotropic slip, which can be seen in the use of posts and some micrograte. Since the lift-up mechanism is reduced by the weakening of the wall shear, the transient growth of perturbations is also reduced. Spanwise slip results in long tilted streamwise structures during transient growth and isotropic slip greatly reduces the amount of linear instability within the flow [16].

1.2.3 Body Force

One method of active control for the turbulent flow includes the use of fluids with increased electrical conductance, which can be applied to both gases and fluids [11]. An electromagnetic wave is then applied in order to induce a motion within the fluid to reduce the amount of drag, demonstrated physically in Figure 3. Others have reported that upwards of 30% skin-friction drag reduction is obtainable when applying the Lorentz force in the transverse direction along the lower wall [17]. Varying the wavelength gives a monotonic trend for drag reduction, where longer wavelengths greatly increase the amount of drag reduction [18]. However, achieving the highest drag reduction might not be the most cost-effective choice since there is not a linear relationship between the amount of net energy savings and the drag reduction achieved [19].

The Lorentz force manipulates the low speed streaks and vortex structures in the longitudinal direction in order to reduce the amount of drag. Turbulent drag is primarily caused by bursting events where streaks lift the low momentum fluid away from the wall. This causes the streaks to become unstable and break apart, known as the burst and is followed by a sweeping event where higher momentum fluid then moves towards the walls. An increase of bursting events can create an increase in the amount of drag at the

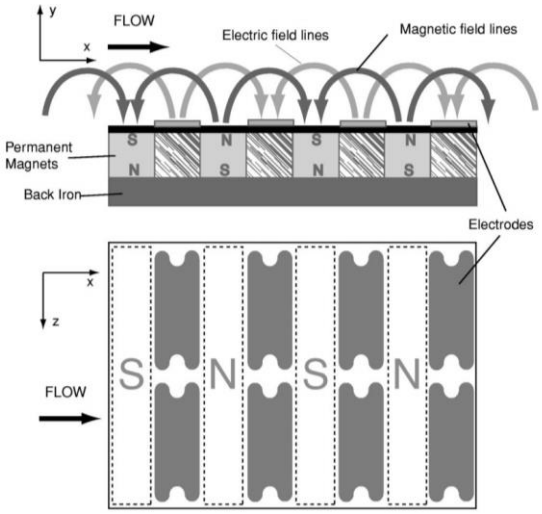

Figure 3: Diagram of experimental body force method setup [20].

wall. The transverse Lorentz force increases the frequency of these bursts, however the bursts are much weaker. Weakening or stabilizing the low speed streaks and vortices assists with the weakening of the bursting events in order to increase the amount of drag reduction [17].

1.2.4 Riblets

Another passive technique involves the use of riblets or microgrooves that have anisotropic properties where the drag reduction varies depending on the height and alignment of the riblets. The riblets force the streamwise vortices away from the wall therefore reducing the amount of shear stress in the near-wall region [21]. In order to maximize the net drag reduction, the shape of the riblets and the distance between them needs to be optimized, otherwise there will be an increase of drag. The different shapes that riblets can take include rectangular, sinusoidal, triangular, and a few more complex shapes as seen in Figure 4. There are multiple causes for drag reduction when using

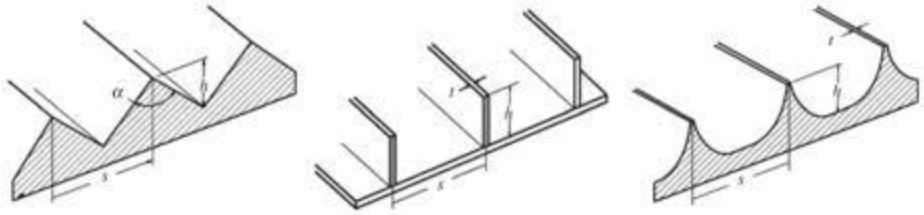

Figure 4: Examples of different riblet formations [22].

riblets such as the lateral spacing of the riblets [23] and the protrusion height [24]. When aligned in the longitudinal direction, it appears that the optimal spacing is approximately 18 wall units with a drag reduction close to 10% [25, 26, 27].

1.2.5 Opposition Control

A form of active control defined as opposition control involves wall-normal blowing and suction in order to control the flow and reduce the amount of drag as demonstrated in Figure 5. When used separately, uniform blowing reduces the skin-friction drag in the system and increases the amount of turbulence where the near-wall vortices are lifted away from the wall, becoming weaker. The opposite effects occur for uniform suction where the drag increases and suppresses the turbulence where the near-wall vortices weaken as they moved towards the wall [28, 29]. Opposition control involves the use of a detection plane in order to determine whether blowing or suction occurs. The blowing and suction at the wall create ejection and sweep events that aim to achieve a net velocity of zero at the detection plane. Opposition control reduces the spinning of the streamwise vortices in order to stabilize them in space [30]. When blowing and suction are combined at the wall, a drag reduction of 10% can be

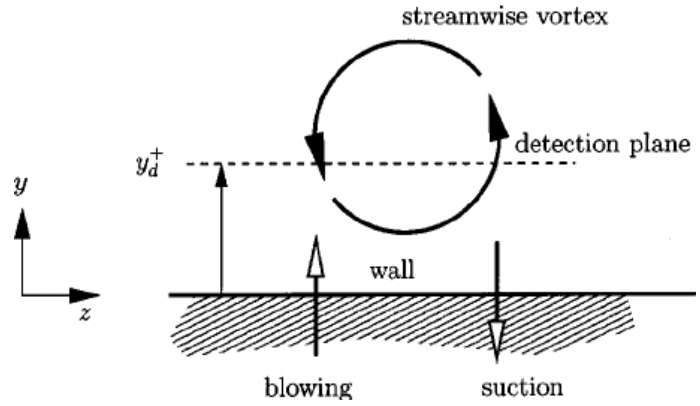

Figure 5: Opposition control method applied at the wall of channel flow [30].

achieved [31]. With certain levels of control input a higher drag reduction of approximately 17% was observed [32].

1.2.6 Wall Movement

Another form of active control is wall movement, for this method the channel walls oscillate in the spanwise direction. The drag reduction rate is primarily determined by the amplitude and frequency of the wall's movement. During this movement, high-speed fluid travels below the low-speed fluid and surrounds the streamwise vortices. Through direct numerical simulations, drag reductions up to 40% can be achieved when the amplitude and frequency are full optimized. Others have found that the friction factor can be reduced by approximately 25% when using circumferential wall oscillation [33]. Wall movement in the streamwise direction has been found to be less effective in reducing the amount of drag, therefore the spanwise direction is preferred. Depending on the setup of the walls and their speed, a travelling wave can be obtained from their

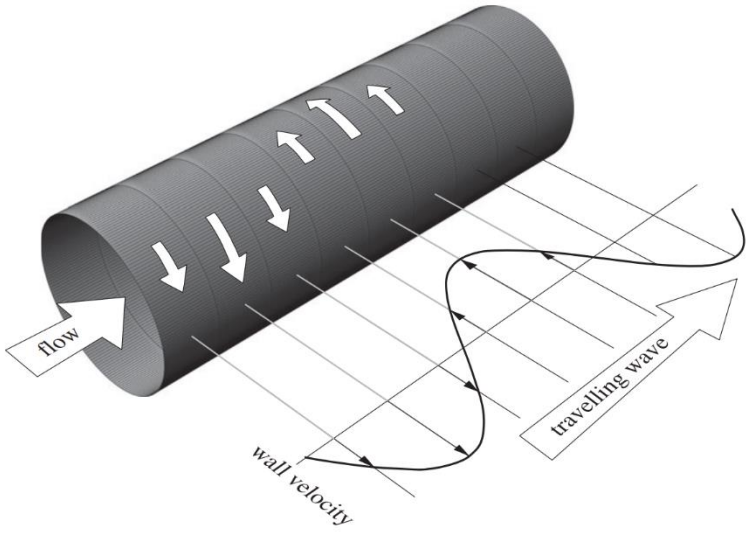

Figure 6: Experimental setup of cylindrical wall movement to create a travelling wave [34].

motion similar in the Lorentz Force as seen in the body force control method. An experimental example of this process can be seen in Figure 6 [35].

1.3 Contributions of This Thesis

The gross effects and structural understanding of drag reduction mechanisms of the flow-control strategies have been well-documented. Recently, Xi and Graham [36] employed the use of temporal analysis in order to investigate the viscoelastic control method. By adapting this temporal analysis, we can elucidate the underlying drag-reduction mechanisms of the viscoelastic, slip, and body force control strategies that have yet to be explored until now.

CHAPTER 2: PROBLEM FORMULATION

For direct numerical simulations, we consider an incompressible fluid in a turbulent channel flow (plane Poiseuille) geometry as shown in Figure 7, the flow is driven by a constant volumetric flux Q. The x, y, and z coordinates are aligned with the streamwise, wall-normal, and spanwise directions, respectively. Periodic boundary conditions are imposed in the x and z directions with fundamental periods L_x and L_z, and solid walls are placed at $y = \pm h$, where h is the half-channel height. The laminar centerline velocity for a given volumetric flux is given as $U_c = (3/4)Q/h$. Where h is the half-height of the channel and the U_c is the laminar centerline velocities, these are used as the characteristic length and velocity scales respectively. The nondimensionalized Navier-Stokes equations are then presented as:

$$\nabla \cdot \boldsymbol{u} = 0, \qquad \frac{\partial \boldsymbol{u}}{\partial t} + \boldsymbol{u} \cdot \nabla \boldsymbol{u} = -\nabla p + \frac{\beta}{Re_c} \nabla^2 \boldsymbol{u} + \boldsymbol{f}_{ext}. \tag{2.1}$$

Here, the Reynolds number for the given laminar centerline velocity is defined as $Re_c = U_c h/\nu$, where ν is the kinematic viscosity of the fluid, β is the ratio of the solvent viscosity and the total viscosity (for a Newtonian fluid, $\beta = 1$), and $\boldsymbol{f}_{ext}$ is the external force that can result from a body force or polymer stress in the present study. For viscoelastic flows, the momentum equation in equation (2.1) includes $\boldsymbol{f}_{ext} = (1 - \beta)\, \nabla \cdot \boldsymbol{\tau}_p$, where the polymer stress tensor $\boldsymbol{\tau}_p$ is related to the polymer conformation tensor $\boldsymbol{\alpha}$. This tensor is then expressed through the FENE-P constitutive relation based on bead-spring dumbbells. These polymer conformation and stress tensors are obtained by solving the following equations:

$$\frac{\partial \boldsymbol{\alpha}}{\partial t} + \boldsymbol{u} \cdot \nabla \boldsymbol{\alpha} - \boldsymbol{\alpha} \cdot \nabla \boldsymbol{u} - (\boldsymbol{\alpha} \cdot \nabla \boldsymbol{u})^T = -\frac{1}{Wi} \boldsymbol{\tau}_p, \qquad \boldsymbol{\tau}_p = \frac{\boldsymbol{\alpha}}{1 - tr(\boldsymbol{\alpha})/b} - \boldsymbol{I}. \tag{2.2}$$

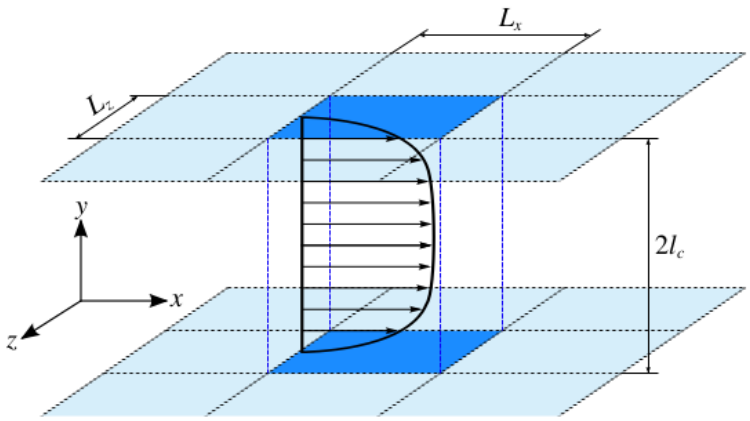

Figure 7: Geometry of the channel flow where the highlighted section is the simulation box and the other sections are its periodic images.

Here, the Weissenberg number is defined as $Wi = \lambda U_c/h$, where λ is the polymer relaxation time, and b is the maximum extensibility of the polymers. For the current study, we fix $\beta = 0.97$ and $b = 10,000$. Since $1 - \beta$ is proportional to polymer concentration and b to the number of monomer units, this parameter set corresponds to a dilute solution of a high molecular-weight polymer. For slip surfaces, the streamwise Navier slip conditions $u_s = L_s\dot{\gamma}_w$ are applied at both top and bottom walls, where L_s is an effective homogeneous slip length and $\dot{\gamma}_w$ is the shear rate at the wall. For an external body force, the following spanwise body force is used for the external force term in equation (2.1):

$$f_z = Ie^{-y/\Delta} \sin\left(\frac{2\pi}{\lambda_z}z - \frac{2\pi}{T}t\right), \tag{2.3}$$

where I is the amplitude of excitation, Δ is the penetration depth, λ_z is the wavelength, and T is the period of oscillation. For inner units, the characteristic inner scales are the friction velocity $u_\tau = \left(\frac{\bar{\tau}_w}{\rho}\right)^{1/2}$ and the near-wall length scale or wall unit $\delta_\nu = \nu/u_\tau$,

where ρ is the fluid density and $\bar{\tau}_w$ is the time- and area-averaged wall shear stress. The quantities nondimensionalized by these inner scales are denoted with a superscript "+". The friction Reynolds number is then defined as $Re_\tau = u_\tau h/\nu = h/\delta_\nu$. Simulations are performed using the open-source code ChannelFlow written and maintained by Gibson [37]. In this study, we focus on the domains of $L_x \times L_y \times L_z = 2\pi \times 2 \times \pi$. A numerical grid system is generated on $N_x \times N_y \times N_z$ (in x, y, and z) meshes, where a Fourier-Chebyshev-Fourier spectral spatial discretization is applied to all variables. A typical resolution used is $(N_x, N_y, N_z) = (48, 81, 48)$. The numerical grid spacing in the streamwise and spanwise direction are $\Delta x^+_{min} \approx 11.0,\ \Delta z^+_{min} \approx 5.5$. The nonuniform Chebyshev spacing used in the wall-normal direction results in $\Delta y^+_{min} \approx 0.05$ at the wall and $\Delta y^+_{max} \approx 2.5$ at the channel centre. For simulations, $Re_c = 1800$ or $Re_\tau = 85$ is being considered.

CHAPTER 3: RESULTS AND DISCUSSION

3.1 Drag Reduction by Control Strategies

From the skin-friction coefficients calculated from each control method as shown in Figures 8(a) and (b), the drag reduction percentage can be defined as DR% $= (C_{f,un} - C_f)/C_{f,un} \times 100\%$, where $C_f = 2\bar{\tau}_w/(\rho U_b^2)$ is the skin-friction coefficient for the controlled case and $C_{f,un}$ is the friction factor for the uncontrolled case. Here, $\bar{\tau}_w$ is the time-area averaged wall shear stress, U_b is the bulk fluid velocity, and ρ is the density, which are all kept constant within the simulations. The error bars on the plots

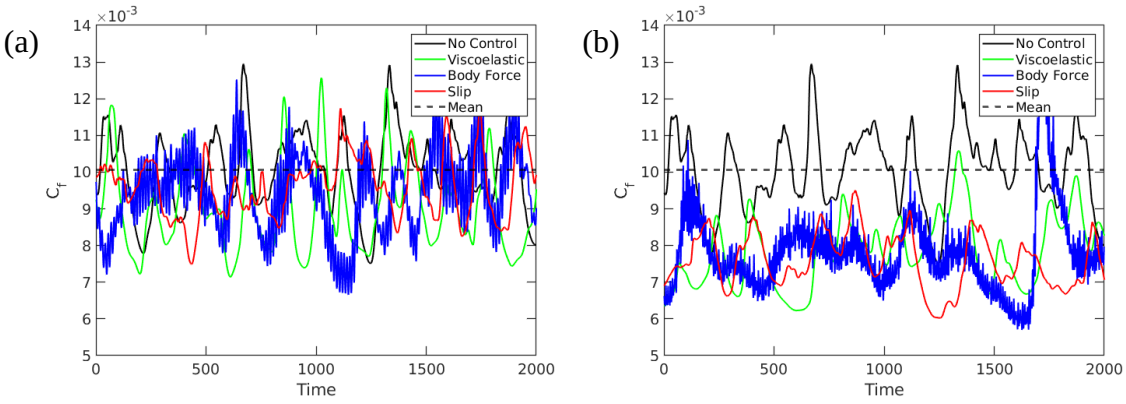

Figure 8: Skin-friction coefficient versus time for (a) DR% = 7% and (b) DR% = 25% states for the no-control method (black), viscoelastic (green), body force (blue), and slip (red). The horizontal dashed line (black) is the mean value of the coefficient of friction for the no-control method.

are the standard errors of the time-averaged quantity with the block-averaging method [38].

Figure 9 shows the drag reduction percentage for viscoelastic turbulence as a function of the Weissenberg number Wi. The results are in good agreement with the previous studies with regard to drag reduction amounts and onset Wi for drag reduction [36, 39].

Figure 10 shows the drag reduction percentages for slip surfaces as a function of L_s. At a fixed Reynolds number, the slip length and drag reduction percentage are almost linearly correlated, which is also observed in Min & Kim [15]. It is worth noting that the largest is $L_s^+ \approx 5$ for the current study, which ensures that the homogeneous slip surface employed in the present study would produce essentially the same outcomes with a heterogeneous microtextured slip surface or superhydrophobic surface [40, 41].

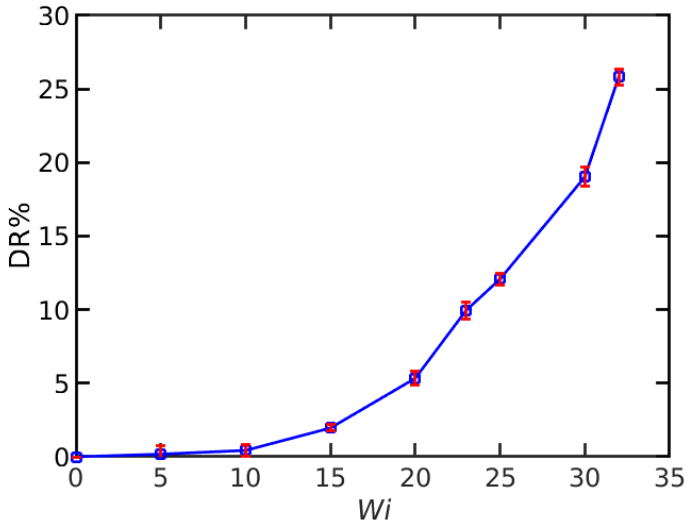

Figure 9: Drag reduction percentages (DR%) versus the Weissenberg number (*Wi*) using the viscoelastic simulation data at $\beta = 0.97$ and $Re_c = 1800$ ($Re_\tau = 85$). The error bars represent the standard error.

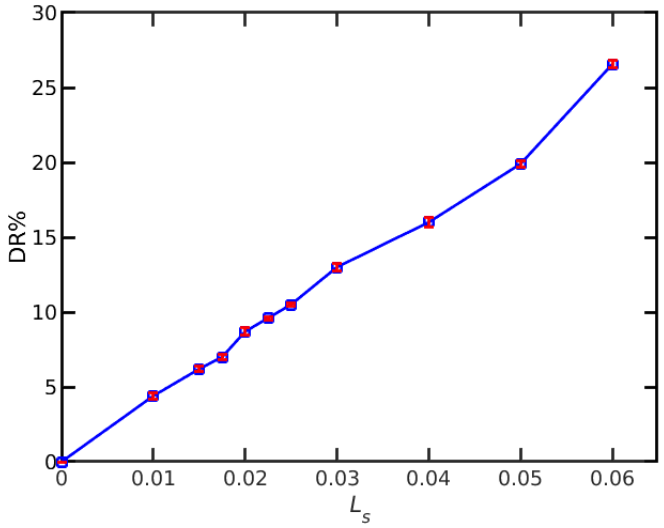

Figure 10: Drag reduction percentages (DR%) versus the effective slip lengths (L_S). The error bars represent the standard error.

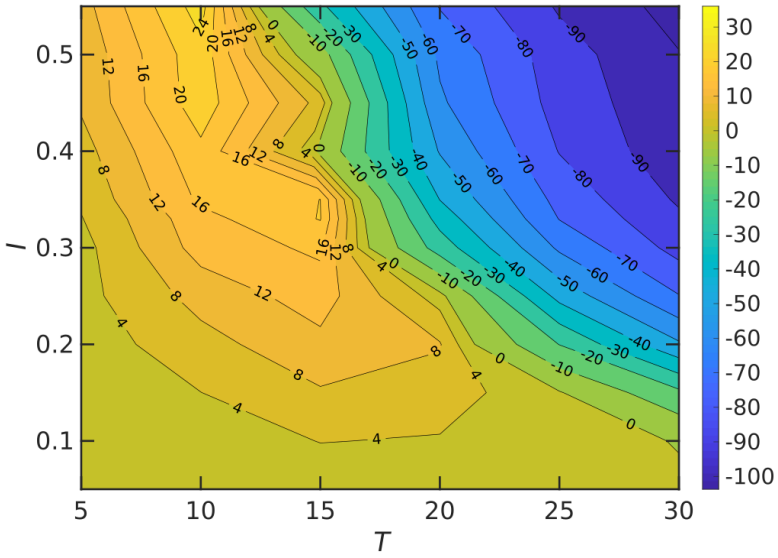

Figure 11: Drag reduction percentages for the body force case by varying the parameters amplitude of excitation (I) and time period of oscillation (T). Where the penetration depth ($\Delta = 0.03$) and the wavelength for the traveling wave $\left(\lambda_z = \frac{\pi}{2}\right)$ are held constant.

Figure 11 shows the drag reduction percentages for body forces for various values of the amplitude of excitation (I) and the time-period of oscillation (T), where we fix the penetration depth $\Delta = 0.03 (\Delta^+ = 2.6)$ and wavelength $\lambda_z = L_z/2 = \pi/2$. Within parameters studied, the maximum drag reduction percentage is approximately 25% at $I = 0.55$ and $T = 10$. At certain parameters there appears to be an increase of drag within the system, as seen in the top right of Figure 11 where the drag increases to over 100%, where it is doubled.

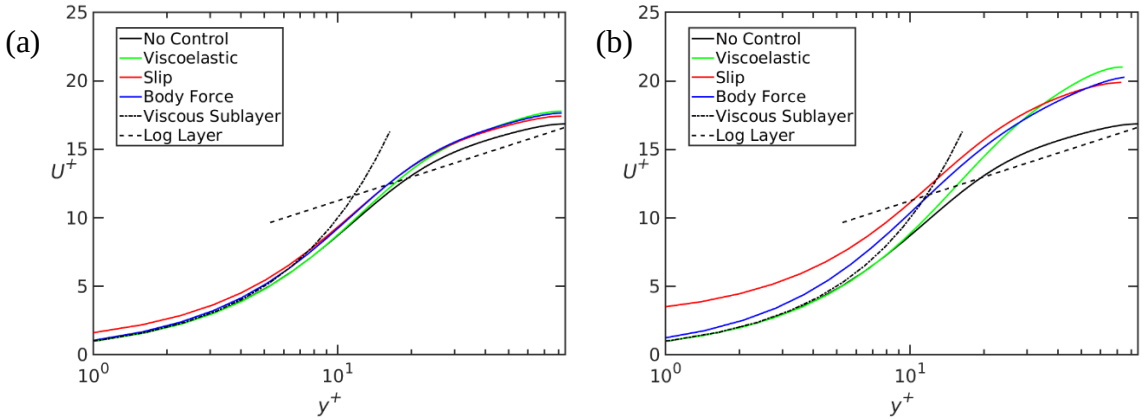

Figure 12: Mean velocity profiles for the no-control (black), viscoelastic (green), slip (red), and body force (blue) methods versus the distance away from the wall in outer units for the different control cases at (a) LDR and (b) HDR. Viscous sublayer, $U^+ = y^+$, is represented by the dotted black line and the log-law layer, $U^+ = 2.5\ln(y^+) + 5.5$, by the black dashed line.

3.2 Drag Reduction Regimes

The mean velocity profiles seen in Figures 12(a) and (b), both uncontrolled and controlled, in inner units are shown at the drag reduction percentages of DR% = 7% and 25%, respectively. For comparison, the profiles for the viscous sublayer $U^+(y^+) = y^+$ and the log-law layer $U^+ = 2.5\ln(y^+) + 5.5$ are also presented. For DR% = 7%, the polymer and body force methods follow the viscous sublayer profile well ($y^+ \leq 5$), while the slip case starts off with a greater velocity than the other two methods due to the slip velocity at the wall. The control profiles begin to slightly deviate from the no-control profile in the buffer layer at $y^+ \approx 20$. The no-control profile lies closer to the log-law profile, but it is placed just above the log-law profile because of the effects of low Reynolds number [42]. The velocity profiles of the three control methods are elevated beyond the no-control and are very close to one another, suggesting almost the same

lower drag. For DR% = 25%, the mean velocity profiles of the polymer and body force methods clearly diverge from the log-law slope with a steeper incline. The slip profile shows similar values with the other two cases in the log-law layer but with a less steep incline. However, there is a much-increased velocity at the wall due to higher L_s. In Figure 12, the transition from the LDR to the HDR range involves the mean velocity profiles deviating from the log-law slope into a steeper incline which was one of the observable changes noted by Xi and Graham [36].

Regarding the drag reduction percentages, an additional distinction can be applied to separate a low degree of drag reduction (LDR) and a high degree of drag reduction (HDR). Through experimental research, Warholic et al. [43] analyzed the different effects of polymers at high and low drag reduction regimes. They used a Reynolds number of approximately 20,000 and defined their drag reduction as a ratio of τ_w for polymer solution to τ_w of water. At lower drag reduction percentages, the mean velocity profiles follow a logarithmic profile close to $U^+ = 2.41 \ln(y^+) + 5.5$. At higher drag reduction percentages, the mean velocity profile does not retain this same behavior. They found that at a drag reduction of 33%, there was a weak correlation to this log behavior and as the drag reduction percentage increased the mean velocity profile became closer to the Maximum Drag Reduction asymptote, $U^+ = 11.7 \ln(y^+) - 17$. Warholic et al. also observed the differences in Reynolds shear stress behaviors from both the low and high drag reduction regimes [43]. From this research, many papers used 0-30% drag reduction as LDR, 30-40% as a more transitional region, and drag reduction greater than 40% as HDR for their definitions for LDR and HDR.

The paper by Zhu and Xi [9] further discussed the topic of low- and high-extent drag reduction regimes through analyzing numerous simulations. They found the transition from LDR to HDR occurred around approximately DR = 20% and Wi = 24 at $Re_\tau = 172.31$, here the mean velocity profile breaks away from the logarithmic behavior and the Reynolds shear stress begins to decrease significantly. They noted that the transition point of 20% drag reduction varies with the Reynolds number used, as the Re value increases so will this transitional point from LDR to HDR which can describe the higher percentage values that Warholic *et al.* had observed [9]. In another paper by Zhu and Xi, their onset of drag reduction for $Re_\tau = 86.15$ started before Wi = 10 and the transition from LDR to HDR began at Wi = 24 which corresponds to our data at $Re_\tau = 85$ [44].

The paper by Xi and Graham [36] discusses various ranges for low and high drag reduction regimes, where LDR is below 13% and HDR is above 15% drag reduction. Our drag reduction data can be divided into similar sections where the LDR cases are approximately 7% and HDR is at 25% drag reduction. According to Xi and Graham during the transition from the LDR to the HDR range, there are three observable changes that occur. The two changes that are currently observed in our data include the divergence of the mean velocity profile from the log-law slope into a steeper incline and the suppression of the Reynolds shear stress profile [45]. Thus, the 7% and 25% drag reduction cases belong indeed to the LDR and HDR regimes, respectively, where the steeper mean velocity profile slope distinguishes the HDR regime from the LDR regime.

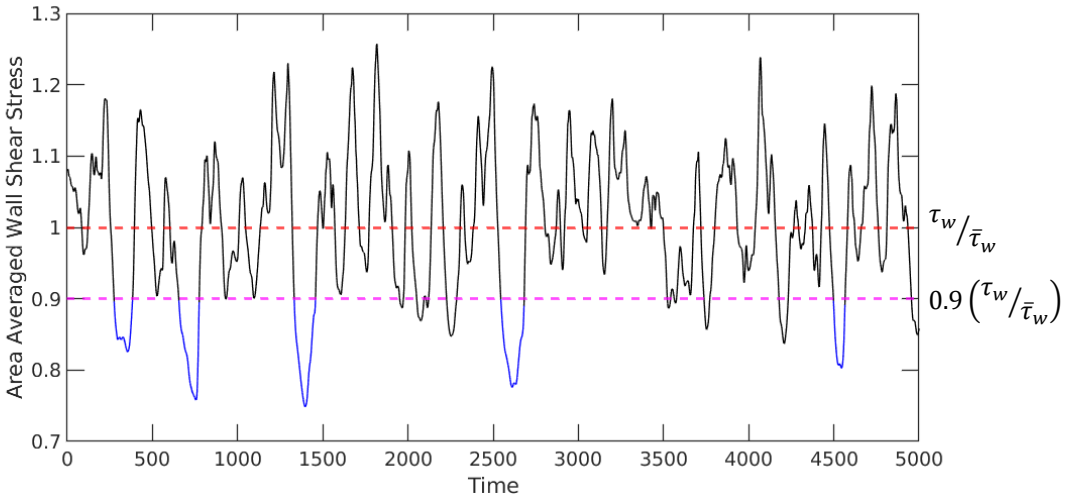

Figure 13: Normalized area averaged wall shear stress from the bottom channel wall for the no-control case vs. nondimensionalized units for time. The dashed line (red) represents the mean wall shear stress and the dotted line (magenta) is 90% of the mean wall shear stress.

3.3 Temporal Analysis to Underlying Drag-Reduction Mechanisms

3.3.1 Hibernating and Active Turbulence

We now aim to describe the underlying drag-reduction mechanisms based on a temporal characterization of temporal events with varying amounts of drag relative to the mean. It has been seen that a turbulent flow is observed to intermittently fluctuate between low and high friction drag, which can be seen in Figure 13. During a low-drag period, vortical motions are suppressed with less wavy low-speed streaks, causing low Reynolds shear stress [8]. These low drag intervals are termed hibernating turbulence [45]. The periods between the hibernating intervals are called active turbulence and display high-drag features. The criteria for hibernating turbulence involve the wall shear stress remaining below 90% of its mean value for at least three eddy turnover times

($> \Delta t u_\tau/h = 3$) [46, 47]. We already addressed the issue of sensitivity to the chosen values and showed almost identical results (Kushwaha et al. 2017; Park et al. 2018). To quantify the effects of the flow-control methods on the temporal intermittency of turbulence, the duration and frequency of hibernating and active turbulence are computed from simulation runs for $T = 150000\ h/U_c$ ($> 80Re_c$) for all cases. The average duration of hibernating and active turbulence and the fraction of time spent in hibernation (T_H, T_A, F_H, respectively) are calculated as:

$$T_H = \frac{\sum_{i=1}^{N_H} t_{H,i}}{N_H}, \qquad T_A = \frac{\mathrm{T} - \sum_{i=1}^{N_H} t_{H,i}}{N_A}, \qquad F_H = \frac{\sum_{i=1}^{N_H} t_{H,i}}{\mathrm{T}}, \tag{3.1}$$

where $t_{H,i}$ is the duration of the ith hibernating interval, and N_H and N_A are the total number of hibernating and active intervals over the total duration of the simulation T, respectively. Specifically, F_H can be referred to as a temporal intermittency factor for low friction drag [46]. For temporal investigations, these three quantities T_H, T_A, and F_H are considered along with the average number of hibernations n_H over $30{,}000\ h/U_c$ for the LDR and HDR regimes in comparison to no-control case.

Figure 14(a) was produced by calculating the average duration of hibernating and active turbulence along with the fraction of hibernation for the viscoelastic case at various Weissenberg numbers at $\beta = 0.97$ and $Re_c = 1800$ ($Re_\tau = 85$). Similar to the data represented in the paper by Xi & Graham, the hibernating turbulence remained relatively constant, while active turbulence decreased, as the Weissenberg number increases. As a result, the fraction of hibernation greatly increases after the critical Weissenberg number of approximately 17 [36]. From Figure 14, there is a correlation between the fraction of hibernation and drag reduction since they are very similar to each

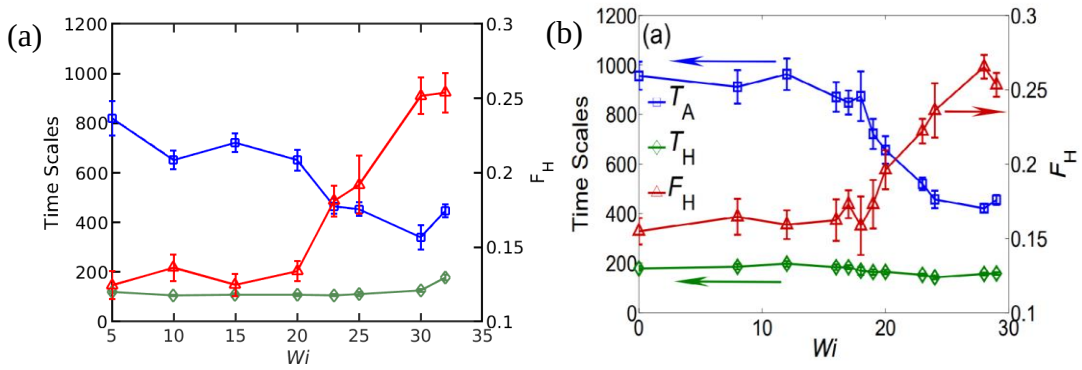

Figure 14: (a) Viscoelastic simulation data at $\beta = 0.97$ and $Re_c = 1800$ ($Re_\tau = 85$). Duration of hibernating and active intervals T_H and T_A respectively (left axis), and fraction of hibernation F_H (right axis), are plotted against the Weissenberg number. (b) From the paper by Xi & Graham [48].

other. The increase of the viscoelasticity in the fluid only effects the duration of active intervals, while having no effect on the hibernating intervals. Since our data follows a similar trend as Xi and Graham [48] from Figure 14(b), we are able to continue with the analysis of hibernating and active turbulence to analyze the mechanisms of different control methods [45].

3.3.2 Low Drag Reduction Regime

Figure 15 shows the temporal quantities for a drag reduction of 7% at the LDR regime. It appears that the polymer and slip methods share similar characteristics. They show almost the same duration of hibernating intervals as the no-control case but a decrease in the duration of active intervals. These changes lead to an increase in the fraction of hibernation and the number of hibernations compared to the no-control case. These trends are in good agreement with the previous studies on viscoelastic turbulence

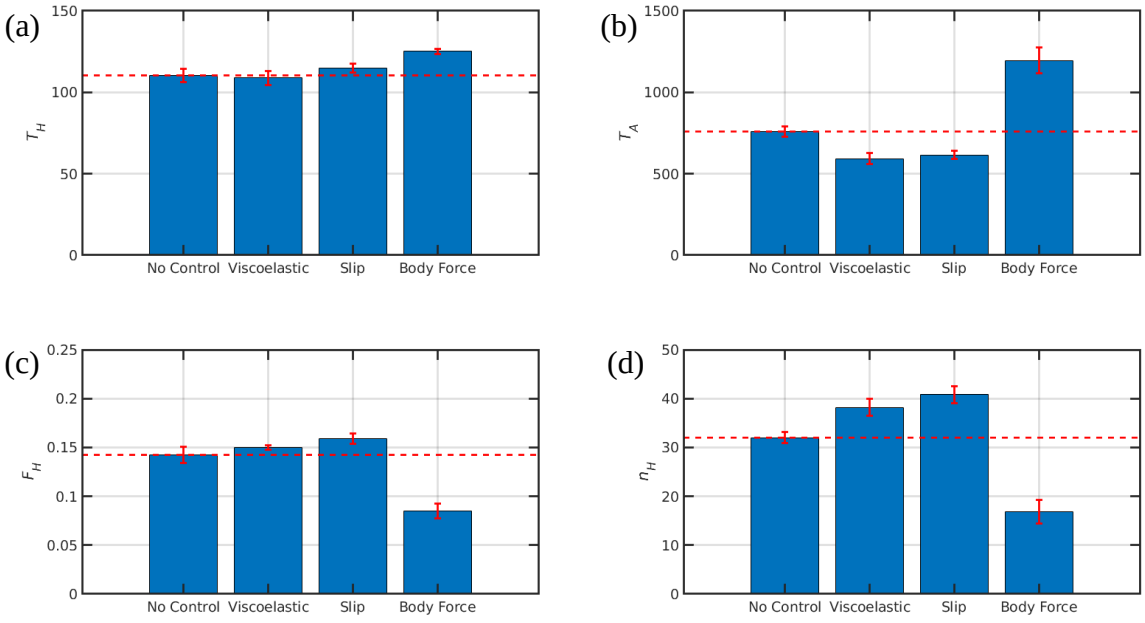

Figure 15. Temporal data at DR% = 7% (LDR): (a, b) the average duration of hibernating and active turbulence, respectively, (c) the fraction of hibernation, and (d) the average number of hibernations over 30000 h/U_c. The results are from viscoelastic ($Wi = 20$), slip ($L_s = 0.015$), and body force ($I = 0.15, T = 15$) cases. The dashed (red) line represents the no-control case's values for better visualization of changes that occur. The error bars represent the standard error.

at low Wi [36, 39]. However, the body force method shows different behaviors, where the duration of both hibernating and active intervals increases, while the fraction of hibernation and the average number of hibernations decrease compared to the no-control values. These trends might indicate that the body force method could cause a drag increase rather than a drag reduction of 7% even though T_H is larger than the no-control value. Thus, it is strongly suggested that the body force method is likely to have a different drag-reduction mechanism compared to the polymer and slip methods at the LDR regime.

3.3.3 High Drag Reduction Regime

Figure 16 shows the different control cases for a drag reduction of 25% at the HDR regime. As in the LDR regime, the polymer and slip control methods display similar behaviors. While the trends of T_A, F_H, and n_H with respect to the no-control case are similar to the LDR cases, the average duration of hibernating turbulence does increase and is now larger than the no-control value. With this increase in T_H and the resulting increase in F_H, a much higher drag reduction ($\sim$25%) is achieved. For the body force method, the trend is still similar to its LDR case but shows more noticeable changes in the quantities. In comparison to the LDR case, T_H and T_A become almost doubled, while F_H remains almost the same, and n_H decreases slightly. These trends still might indicate that the body force method could cause a drag increase rather than a drag reduction of 25%. Thus, a different drag reduction mechanism could be suggested for the body force method compared to the polymer and slip methods even at the HDR regime.

With the temporal quantities at the LDR and HDR regimes, the underlying drag reduction mechanisms can be made for the control methods being investigated. As seen above, it appears that the mechanism is almost the same for polymer and slip methods. For LDR, they achieve a drag reduction by decreasing the duration of active intervals, while the duration of hibernating turbulence remains almost constant. These trends lead to more frequent hibernation and an increase in the temporal intermittency factor. For HDR, while they still show a decrease in the duration of active turbulence, a more drag reduction is achieved by increasing the duration of hibernating turbulence, which results in a more increase in F_H compared to the LDR case. Interestingly, the body force method displays a distinctly different mechanism at both LDR and HDR regimes. Although it

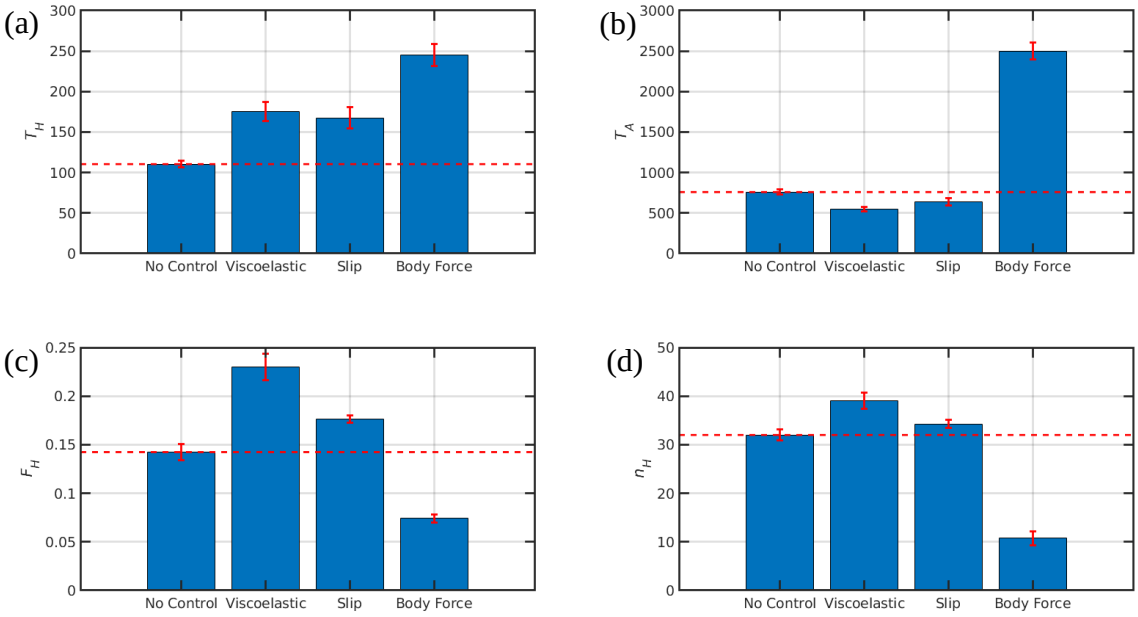

Figure 16: Temporal data at DR% = 25% (HDR): (a, b) the average duration of hibernating and active turbulence, respectively, (c) the fraction of hibernation, and (d) the average number of hibernations over 30000 h/U_c. The results are from viscoelastic ($Wi = 31$), slip ($L_s = 0.06$), and body force ($I = 0.55, T = 10$) cases. The dashed (red) line represents the no-control case's values for better visualization of changes that occur. The error bars represent the standard error.

causes less frequent hibernation and even a smaller F_H value than the no-control case, the highly prolonged hibernation intervals are likely to produce comparable amounts of drag reduction to the polymer and slip methods.

3.4 Mechanisms Behind Flow-Control Strategies

3.4.1 Reynolds Shear Stress

Lastly, we attempt to illuminate the mechanisms behind the different temporal characteristics for drag reduction between the polymers/slip methods and body force

method. It has been shown that the effects of flow-control methods on the Reynolds shear stress and vortical structures may provide a mechanistic basis for drag reduction in turbulent flows [4, 5]. Figures 17(a) and (b) depict the time averaged Reynolds shear stress profiles of the different control methods along with no-control case for the LDR and HDR regimes, respectively. For LDR, the three control profiles are slightly lower than the no-control case. It is observed that the body force profile is slightly higher than the polymers/slip and no-control profiles in $y^+ < 15$. For HDR, the three control profiles are fairly reduced compared with the magnitudes of the no-control profile. The slip profile is still relatively close to the no-control case compared to the other two cases. More interestingly, a change in the shape of the body force profile is noticeable, which is non-monotonic. Mostly, the profile is rather higher than the no-control case in $y^+ < 10$, with the peak being close to $y^+ \approx 7$, and its magnitude falls below the other cases from $y^+ > 18$, with another peak at almost the same locations as the other profiles. Note that this non-monotonic shape is kept even for hibernation and active intervals (not shown), while the magnitudes are different.

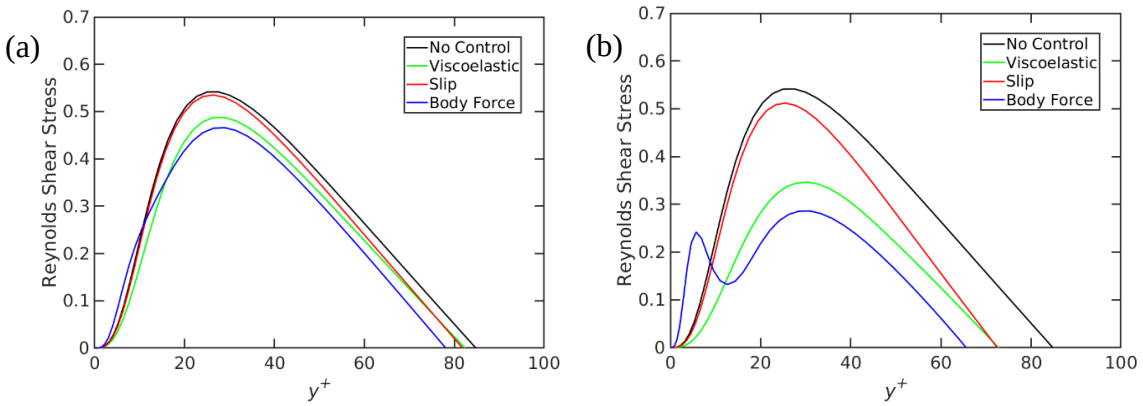

Figure 17: Reynolds shear stress versus the distance from the wall in outer units for the different control methods at (a) LDR and (b) HDR regime.

3.4.2 Vortex Structures

In Figure 18, the vortex structures in the body force control method decrease as the drag reduction increases. There are roller-like vortical structures forming along the bottom due to the body force that is being applied at the bottom wall of the channel. The structures geometry is related to the various parameters in the body force equations. In Figure 19, the slip control method vortex structures have been lifted away from the wall due to the slip condition induced at the channel wall's surface. In Figure 20, the viscoelastic control method shows the vortex structures elongating and becoming more streamline.

To elucidate the seemingly distinct characteristics of the body force method for a drag-reduction mechanism, we plot its vortical structures for which the swirling strength λ_{ci}, the imaginary part of the complex conjugate eigenvalues of the velocity gradient tensor [49], are calculated. Figures 18(a) and (c) show contours of the swirling strength for half of the channel for the LDR and HDR regimes, respectively. The contours represent isosurfaces of 50% of the maximum λ_{ci} for each case. Similar to Mamori & Fukagata [50], the streamwise roller-like structures are clearly observed very close to the wall. As the wavelength of the body force is set to $L_z/2$, four roller-like vortices are formed and separated by $L_z/4$, a pair of vortices per wavelength. It is observed that the heights of these vortices are independent of the choice of the other control parameters such as penetration depth (Δ), force magnitude (I), and period (T). The center of the rollers is located at $y^+ \approx 7$. Given these streamwise-spanned roller-like vortices, it can be speculated that the body force is likely to prevent interactions between the inner region

and outer region by which the hibernation intervals tend to be substantially prolonged. In other words, these streamwise roller-like structures tend to stay near the wall and block structures from the outer region, which helps increase the hibernation intervals for the reduction of friction drag. The differences in Reynolds shear stress and vortical structures between the polymer/slip methods and the body force method may provide clear and plausible mechanisms responsible for distinct underlying drag-reduction mechanisms, for which further investigation is yet needed.

The streaks observed in Figure 18 are defined by the wavelength of the body force, in this case $\lambda_z = \frac{\pi}{2}$. From the wavelength, there are two periods displayed in the domain which corresponds to the four streaks seen in the figure, two streaks per period. The streaks alternate height, for example the streak on the far left will be centered at 0.08 outer units from the bottom wall and the next one will be at 0.12 outer units. The streaks primarily appear during low drag events, but do appear during high drag events at HDR. One possible mechanism behind this behavior is that the body force is trying to prolong the low drag event, which will increase the drag reduction. These streak structures try to prevent the outer structures from penetrating into the near-wall area. In other words, the streaks stay there and block other vortex structures from the outer log layer or wake layer, and this helps increase the hibernation intervals and produce more drag reduction.

For a parametric study, the penetration depth (Δ) was increased from 0.03 to 0.06 and 0.09. As the depth was increased the size of the streaks change, where every other streak is decreased in size. The position however does not appear to be altered. As the penetration depth is varied, the drag reduction percentages do not remain monotonic, the

drag reduction fluctuates. For the body force case, there are multiple sets of parameters that can give the same drag reduction percentage, for example three points $(I = 0.15, T = 20)$, $(I = 0.20, T = 10)$, and $(I = 0.40, T = 5)$ all have a drag reduction of 7%. A question arises is if these different parameters have the same T_H, T_A, F_H, and number of hibernations. It appears that there is not a strong correlation between the drag reduction percentage and the T_H, T_A, and F_H values. When comparing simulations with the same parameters, the values obtained can vary from each other.

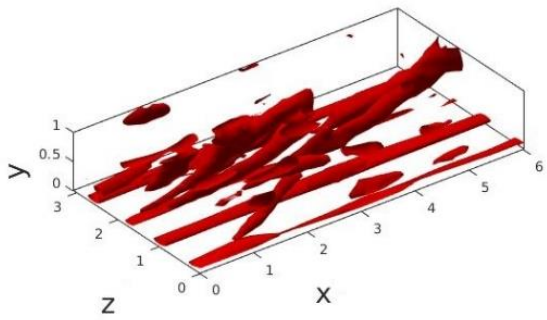

(a) I = 0.15, T = 15, low wall shear stress $\lambda_{ci} = 0.6963$

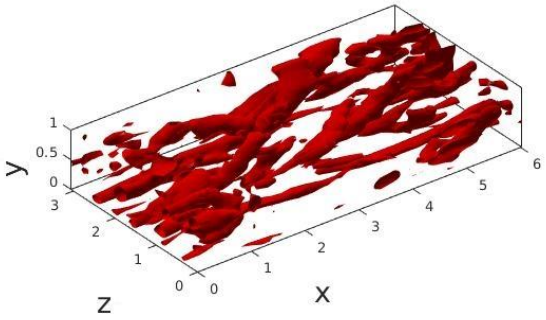

(b) I = 0.15, T = 15, high wall shear stress $\lambda_{ci} = 1.1600$

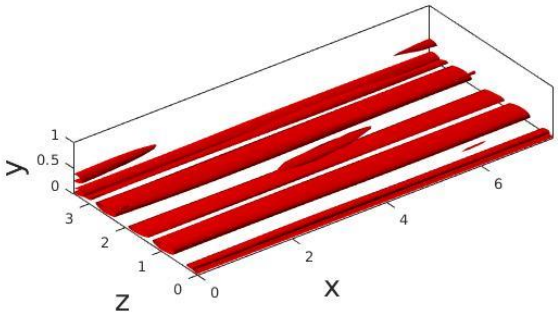

(c) I = 0.55, T = 10, low wall shear stress $\lambda_{ci} = 0.7716$

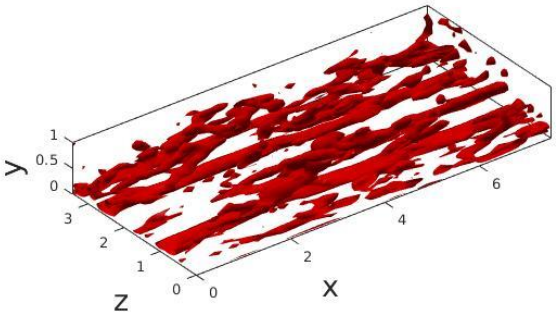

(d) I = 0.55, T = 10, high wall shear stress $\lambda_{ci} = 2.4589$

Figure 18: Vortex structures of the fluid simulations at a single point in time for the body force method at (a-b) LDR and (c-d) HDR.

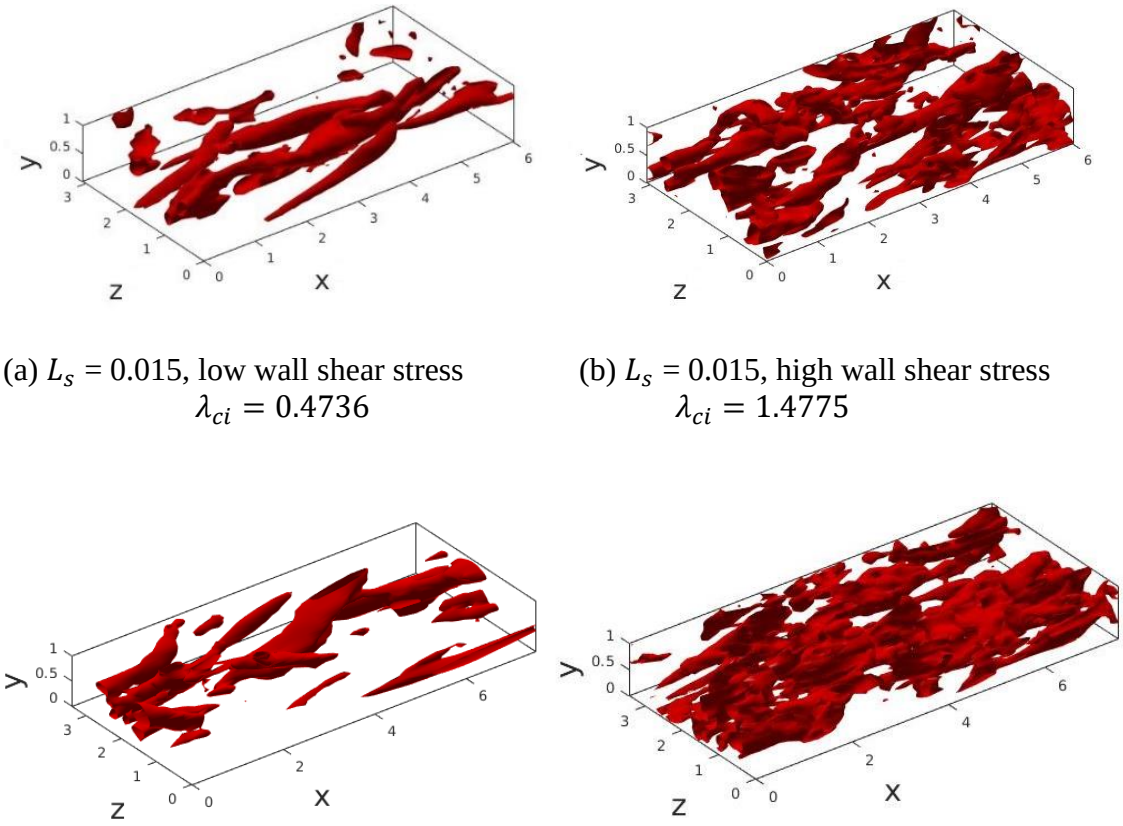

(a) L_s = 0.015, low wall shear stress $\lambda_{ci} = 0.4736$

(b) L_s = 0.015, high wall shear stress $\lambda_{ci} = 1.4775$

(c) L_s = 0.06, low wall shear stress $\lambda_{ci} = 0.3765$

(d) L_s = 0.06, high wall shear stress $\lambda_{ci} = 0.9747$

Figure 19: Vortex structures of the fluid simulations at a single point in time for the slip method at (a-b) LDR and (c-d) HDR.

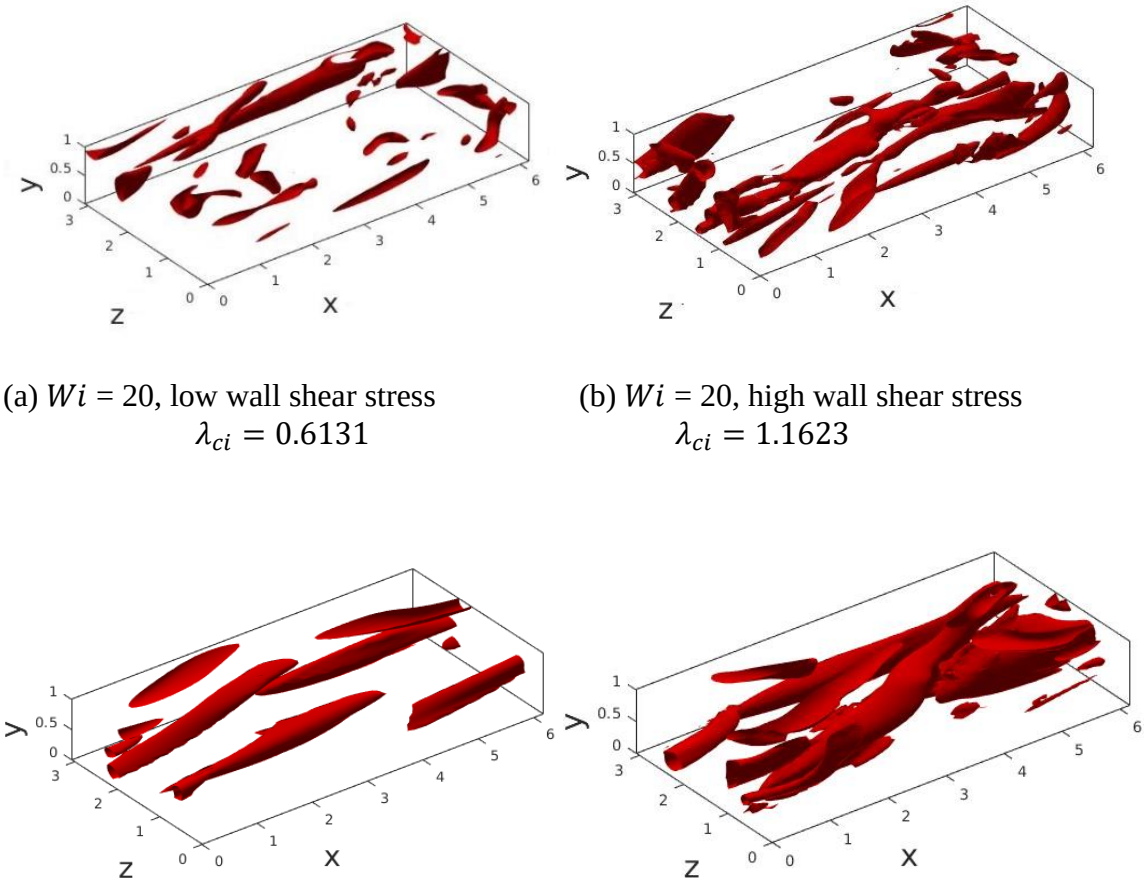

(a) Wi = 20, low wall shear stress
$\lambda_{ci} = 0.6131$

(b) Wi = 20, high wall shear stress
$\lambda_{ci} = 1.1623$

(c) Wi = 31, low wall shear stress
$\lambda_{ci} = 0.3013$

(d) Wi = 31, high wall shear stress
$\lambda_{ci} = 0.3909$

Figure 20: Vortex structures of the fluid simulations at a single point in time for the viscoelastic method at (a-b) LDR and (c-d) HDR.

CHAPTER 4: CONCLUSION AND FUTURE WORK

Through direct numerical simulations in a channel flow (plane Poiseuille) geometry, the underlying drag-reduction mechanisms of three flow-control strategies, namely polymer additives, slip surfaces, and external body forces, are investigated by utilizing two temporal turbulent phases – hibernating and active turbulence [38]. Given similar drag-reduction percentages, the polymers/slip methods demonstrate a similar mechanism to one another by causing the hibernation phases to occur more frequently with a decrease in the duration of active phases. The body force method shows a different mechanism, where the hibernation phases happen less frequently, however the duration of these hibernations is prolonged due to roller-like vortical structures formed near the wall. These vortical structures appear to prevent interactions between the inner and outer regions to make hibernating phases longer. At higher drag-reduction regimes, each control method seems to involve different mechanisms to manipulate the Reynolds shear stress for which follow-up work is under investigation. These distinct underlying drag-reduction mechanisms between the polymers/slip methods and body force method could suggest that different adaptive and optimal flow-control techniques could be used to promote more drag reduction, which will be a subject of interesting future work. Future work for this type of research could involve investigating these drag reducing mechanisms at higher Reynolds numbers. Control methods mentioned in the literature review such as opposition control, riblets, and wall movement can be incorporated into the analysis.

References

[1] S. K. Robinson. Coherent motions in the turbulent boundary layer. *Annu. Rev. Fluid Mech*. 23 (1), 601–639 (1991).

[2] F. Waleffe. On a self-sustaining process in shear flows. *Phys. Fluids* 9 (4), 883–900 (1997).

[3] J. M Hamilton. , J. Kim & F. Waleffe. Regeneration mechanisms of near-wall turbulence structures. *J. Fluid Mech*. 287 (1), 317–348 (1995).

[4] J. Lumley &P. Blossey. Control of turbulence. *Annu. Rev. Fluid Mech*. 30 (1), 311–327 (1998).

[5] M. Gad-el Hak. Flow control: passive, active, and reactive flow management. *Cambridge University press* (2007).

[6] K. Kim, C.-F. Li, R. Sureshkumar, S. Balachandar, & R. J. Adrian. Effects of polymer stresses on eddy structures in drag-reduced turbulent channel flow. *J. Fluid Mech.* (2007).

[7] C. M. White, & M. G. Mungal. Mechanics and prediction of turbulent drag reduction with polymer additives. *Annu. Rev. Fluid Mech*., 40, 235-256 (2008).

[8] M. D. Graham. Drag reduction and the dynamics of turbulence in simple complex fluids, *Phys. Fluids.* 26 1-24 (2014).

[9] L. Zhu and L. Xi. Vortex dynamics in low- and high-extent polymer drag reduction regimes revealed by vortex tracking and conformation analysis. *Phys. Fluids*, 31:095103, (2019).

[10] T. Min, J. Y. Yoo, H. Choi, and D. D. Joseph. Drag reduction by polymer additives in a turbulent channel flow. *J. Fluid Mech*. 486, 213-283.(2003).

[11] G. E. Karniadakis & K.-S. Choi. Mechanisms on transverse motions in turbulent wall flows. *Annu. Rev. Fluid Mech*. 35 (1), 45–62 (2003).

[12] J. P. Rothstein. Slip on superhydrophobic surfaces. *Annu. Rev. Fluid Mech*. 42 (1), 89–109 (2010).

[13] H. Park, H. Park, and J. Kim. A numerical study on the effects of superhydrophobic surface on skin-friction drag in turbulent channel flow. *Phys. Fluids*, 25, (2013).

[14] M. B. Martell, J. P. Rothstein, and J. B. Perot. An analysis of superhydrophobic turbulent drag reduction mechanisms using direct numerical simulation. *Phys. Fluids*, 22:065102, (2010).

[15] T. Min and J. Kim. Effects of hydrophobic surface on stability and transition. *Phys. Fluids*. 17, 088106 (2004).

[16] C. Chai and B. Song. Stability of slip channel flow revisited. *Phys. Fluids*, 31:084105, (2019).

[17] L. Huang, B. Fan, and G. Dong. Turbulent drag reduction via a transverse wave traveling along streamwise direction induced by Lorentz force. *Phys. Fluids*. 22:015103, (2010).

[18] V. Symeonidis, Y. Du, and G. E. Karniadakis. Drag reduction in wall-bounded turbulence via a transverse travelling wave. *J. Fluid Mech*. 457, 1-34 (2002).

[19] M. Albers, P. S. Meysonnat, D. Fernex, R. Semaan, Bernd, R. Noack, and W. Schroder. Drag reduction and energy saving by spanwise traveling transversal surface waves for flat plate flow. *Phys. Fluids*, 105, 125-157 (2019).

[20] Breuer, Park, and Henoch. Actuation and control of a turbulent channel flow using Lorentz forces. *Phys. Fluids*, 16 (4), 897-907 (2004).

[21] R. Garcia-Mayoral and J. Jimenez. Drag reduction by riblets. *Phil. Trans. R. Soc.* 369, 1412-1427 (2011).

[22] N. West, K. Sammut, and Y. Tang. Material selection and manufacturing of riblets for drag reduction: An updated review. *Proc. Inst. Mech. Eng. L-J. Mat.* 232 (7), 610-622 (2016).

[23] R. Garcia-Mayoral and J. Jimenez. Hydrodynamic stability and breakdown of the viscous regime over riblets. *J. Fluid Mech*. 678, 317-347 (2011).

[24] P. Luchini, F. Manzo, and A. Pozzi. Resistance of a grooved surface to parallel flow and cross-flow. *J. Fluid Mech.* 228, 87-109 (1991).

[25] O. A. El-Samni, H. H. Chum, and H. S. Yoon. Drag reduction of turbulent flow over thin rectangular riblets. *Int. J. Eng. Sci*. 45, 436-454 (2007).

[26] M. Sasamori, O. Iihama, H. Mamori, K. Iwamoto, and A. Murata. Parametric Study on a Sinusoidal Riblet for Drag Reduction by Direct Numerical Simulation. *Flow Turb. Combust.* 99 (1), 47-69 (2017).

[27] T. Endo and R. Himeno. Direct numerical simulation of turbulent flow over a compliant surface. *J. Turbul*. 3 (7), 1-10 (2002).

[28] Y. Kametani, K. Fukagata, R. Orlu, and P. Schlatter. Effect of uniform blowing/suction in a turbulent boundary layer at moderate Reynolds number. *Int. J. Heat Fluid Flow*. 55, 132-142 (2015).

[29] J. Park and H. Choi. Effects of uniform blowing or suction from a spanwise slot on turbulent boundary layer flow. *Phys. Fluids* 11 (10), 3095-3105 (1999).

[30] J. Lim and J. Kim. A singular value analysis of boundary layer control. *Phys. Fluids* 16 (6), 1980-1988 (2004).

[31] T. Segawa, H. Mizunuma, K. Murakami, F.-C. Li, and H. Yoshida. Turbulent drag reduction by means of alternating suction and blowing jets. *Fluid Dynamics Research*. 39 (7), 552-568 (2007).

[32] T. Bewley and P. Moin. Optimal control of turbulent channel flows. *ASME* 75, 221-227 (2001).

[33] J. Choi, C. H. Xu, and H. J. Sung. Drag Reduction by Spanwise Wall Oscillation in Wall-Bounded Turbulent Flows. *AIAA* 40 (5), 842-850 (2002).

[34] F. Auteri, A. Baron, M. Belan, G. Campanardi, and M. Qaudrio. Experimental assessment of drag reduction by traveling waves in a turbulent pipe flow. *Phys. Fluids* 22 (11), 115103 (2010).

[35] M. Quardio. Drag reductionin turbulent boundary layers by in-plane wall motion. *Phil. Trans. R. Soc. A* 369, 1428-1442 (2011).

[36] L. Xi and M. D. Graham. Active and Hibernating Turbulence in Minimal Channel Flow of Newtonian and Polymeric Fluids. *Phys. Rev. Lett*. 104, 218301 (2010).

[37] J. F. Gibson. Channelflow: A spectral Navier-Stokes simulator in C++. *Tech. Rep. U.* New Hampshire, Channelflow.org. (2012).

[38] H. Flyvbjerg & H. G. Petersen. Error estimates on averages of correlated data. *J. Chem. Phys*. 91 (1), 461–466 (1989).

[39] Wang, S.-N., Graham, M. D., Hahn, F. J. & Xi, L. Time-series and extended KL analysis of turbulent drag reduction in polymer solutions. *AIChE J.* 60 (4), 1460–1475 (2014).

[40] J. Seo, R. Garcia-Mayoral & A. Mani. Turbulent flows over superhydrophobic surfaces: Flow-induced capillary waves, and robustness of air-water interfaces. *J. Fluid Mech*. 835, 45–85 (2018).

[41] E. A. Davis & J. S. Park. Dynamics of laminar and transitional flows over slip surfaces: effects on the laminar–turbulent separatrix. *J. Fluid Mech*. 894, A16 (2020).

[42] T. Tsukahara, Y. Seki, H. Kawamura & D. Tochio. DNS of turbulent channel flow at very low Reynolds numbers. *In Fourth International Symposium on Turbulence and Shear Flow Phenomena*. Begel House Inc (2005).

[43] M. D. Warholic, H. Massah, T.J. Hanratty. Influence of drag-reduction polymers on turbulence: effects of Reynolds number, concentration and mixing. *Exp Fluids* 27 (5), 461-472 (1999).

[44] L. Zhu and L. Xi. Coherent structure dynamics and identification during the multistage transitions of polymeric turbulent channel flow. *J. Phys.*: *Conf. Ser.*, Vol. 1001, No. 1, p. 01205 (2005).

[45] L. Xi and M. D. Graham. Turbulent drag reduction and multistage transitions in viscoelastic minimal flow units. *J. Fluid Mech*. 647, 421-452 (2010).

[46] A. Kushwaha, J. S. Park & M. D. Graham. Temporal and spatial intermittencies within channel flow turbulence near transition. *Phys. Rev. Fluids* 2 (2), 024603 (2017).

[47] R. Agrawal, H.-H. Ng, E. A. Davis, J. S. Park, M. D. Graham, D. J. Dennis & R. J. Poole. Low- and high-drag intermittencies in turbulent channel flows. *Entropy* 22 (10), 1126 (2020).

[48] L. Xi and M. D. Graham. Intermittent dynamics of turbulence hibernation in Newtonian and viscoelastic minimal channel flows. *J. Fluid Mech*. 693, 433-472 (2012).

[49] J. Zhou, R. J. Adrian, S. Balachandar & T. M. Kendall. Mechanisms for generating coherent packets of hairpin vortices in channel flow. *J. Fluid Mech*. 387, 353–396 (1999).

[50] H. Mamori & K. Fukagata. Drag reduction effect by a wave-like wall-normal body force in a turbulent channel flow. *Phys. Fluids* 26 (11), 115104 (2014).